

ON THE IMPACT OF RANDOM RESIDUAL CALIBRATION ERROR ON THE GIBBS ILC ESTIMATES OVER LARGE ANGULAR SCALES

VIPIN SUDEVAN¹, RAJIB SAHA¹

Draft version January 10, 2020

ABSTRACT

Residual error in calibration coefficients corresponding to observed CMB maps is an important issue while estimating a pure CMB signal. A component separation method, if these errors in the input foreground contaminated CMB maps are not properly taken into account, may lead to bias in the cleaned CMB map and estimated CMB angular power spectrum. But the inability to exactly determine the calibration coefficients corresponding to each observed CMB map from any CMB experiment makes it very difficult to incorporate their exact and actual values in a component separation analysis. Hence the effect of any random and residual calibration error on the cleaned CMB map and its angular power spectrum of a component separation problem can only be understood by performing detailed Monte Carlo simulations. In this paper, we investigate the impact of using input foreground contaminated CMB maps with random calibration errors on posterior density of cleaned CMB map and theoretical CMB angular power spectrum over large angular scales of the sky following the Gibbs ILC method proposed by Sudevan & Saha (2018b). By performing detailed Monte Carlo simulations of WMAP and Planck temperature anisotropy observations with calibration errors compatible with them we show that the best-fit map corresponding to posterior maximum is minimally biased in Gibbs ILC method by a CMB normalization bias and residual foreground bias. The bias in best-fit CMB angular power spectrum with respect to the case where no calibration error is present are $\sim 28\mu K^2$ and $-4.7\mu K^2$ respectively between $2 \leq \ell \leq 15$ and $16 \leq \ell \leq 32$. The calibration error induced error in best-fit power spectrum causes an overall 6% increase of the net error when added in quadrature with the cosmic variance induced error.

Subject headings: cosmic background radiation — cosmology: observations — diffuse radiation, Gibbs Sampling, calibration errors

1. INTRODUCTION

In the era of precision cosmology, for CMB temperature anisotropy and over large angular scales, it is no longer the sensitivity of the detectors but the presence of astrophysical foregrounds and instrumental systematics which hinder the measurement of a pure CMB signal. An accurate CMB signal is essential for better understanding the geometry (Ade et al. 2016a), composition of the universe (Goldstein et al. 2003) and renders stringent constraints on cosmological parameters (Ade et al. 2016c; Hinshaw et al. 2013; Aghanim et al. 2018b). A systematic study of the residual systematic errors on top of the already challenging task of foreground removal from CMB maps is of even more importance for a component separation method with many planned next generation CMB missions (Kogut et al. 2011; André et al. 2014; Hanany et al. 2019; Sutin et al. 2018; Di Valentino et al. 2018; Kogut et al. 2016), which will be designed to detect the signature of very weak primordial gravitational waves, an artifact of the initial inflation of the universe.

Apart from the presence of foreground contamination in the observed maps due to emissions by various astrophysical sources, the presence of residual and random calibration errors poses as a difficult challenge while estimating a pure signal. Although these residual calibration errors may be small in a CMB experiment, their presence implies that it is not possible to obtain exact values of calibration coefficients corresponding to observed CMB map of each detector. The Planck consortium, for example, after using advanced photometric calibration techniques like spin-synchronous modulation of

the CMB orbital dipole (Adam et al. 2016a; Ade et al. 2016b; Akrami et al. 2018) for Low-Frequency instrument (LFI) and by using models of planetary atmospheric emissions and time-variable CMB orbital dipole (Adam et al. 2016b; Aghanim et al. 2018a) for High-Frequency Instrument (HFI) maps, has constrained the calibration uncertainties in the Planck full-sky surveys. They provided stringent limit of 0.024% calibration error at HFI 353 GHz Akrami et al. (2018); Aghanim et al. (2018a) Planck map and $\simeq 1\%$ and $\sim 1.4\%$ calibration error for HFI 545 Aghanim et al. (2018a) and HFI 857 Adam et al. (2016b) Planck maps respectively. Similarly WMAP used the dipole modulation of the CMB signal due to the observatory's motion around the Sun (Jarosik et al. 2011; Hinshaw et al. 2003; Bennett et al. 2013) as a means to calibrate its maps. But it is impossible to determine the exact value of the calibration coefficient corresponding to each individual map. Not accounting for such calibration errors in the observed maps during foreground minimization procedure leads to bias while estimating a cleaned CMB signal (Dick et al. 2010). It is therefore natural to ask, what would be the impact of using such improperly calibrated foreground contaminated CMB maps as inputs to a foreground minimization algorithm on the final cleaned CMB map and its angular power spectrum. In this article, we focus our study on Gibbs ILC CMB reconstruction method (Sudevan & Saha 2018b), which possesses various interesting properties as far as CMB reconstruction by removing foregrounds is concerned as described briefly in the following discussions and in other references mentioned therein.

In order to remove the foregrounds from CMB observations performed by various satellite missions there exist various (foreground) model dependent and independent methods.

¹ Physics Department, Indian Institute of Science Education and Research Bhopal, Bhopal, M.P, 462023, India.

Since CMB and different astrophysical components have different emission laws, a component separation method can utilize these differences to separate the CMB from foregrounds. An important CMB reconstruction method is the Internal-Linear-Combination (ILC) method (Tegmark & Efstathiou 1996; Tegmark et al. 2003; Bennett et al. 2003; Saha et al. 2006) where in order to obtain a cleaned CMB signal, it is neither required to explicitly model the individual foreground component's physical morphology in the form of templates at some reference frequencies nor in the form of corresponding frequency spectra. The method is based on the assumption that the frequency spectra of the foregrounds are different from the frequency spectrum of the CMB, which is assumed to be black-body in nature (Mather et al. 1994; Fixsen et al. 1996). In the ILC method, a cleaned CMB map is obtained by linearly combining multi-frequency observed foreground contaminated CMB maps using some amplitude terms known as weight factors. These weights follow a constrain that their sum should be unity and can be estimated analytically by performing a constrained minimization of the variance of the cleaned CMB map.

In recent years the ILC method has been investigated extensively (Hinshaw et al. 2007; Eriksen et al. 2004; Saha 2011; Saha & Aluri 2016; Sudevan et al. 2017). Sudevan & Saha (2018a) proposed a global ILC method in pixel space by taking into account prior information of CMB covariance matrix under the assumption that detector noise can be ignored over the large angular scales of the sky. Sudevan & Saha (2018b) proposed a method to estimate the CMB posterior density and CMB theoretical angular power spectrum given the observed data over the large angular scales of the sky in a (foreground) model independent manner using the ILC method discussed in Sudevan & Saha (2018a) implemented in harmonic space. They provided the best fit estimates of both, CMB map and theoretical angular power spectrum along with their confidence interval regions and estimated CMB posterior without any need of explicitly modeling the foreground components. The theoretical power spectrum results and its error estimates can directly be integrated to cosmological parameter estimation process.

In Section 2, we review the basic idea of Gibbs ILC method. In Section 3 we discuss how the calibration errors affect the cleaned CMB map. We describe our Monte Carlo simulations to study the effect of calibration errors in Section 4 and show the simulation results in Section 5. In Section 6 we discuss our results and conclude.

2. FORMALISM

In Sudevan & Saha (2018b), we outlined in detail the formalism of the Gibbs ILC method which was implemented in harmonic space at large angular scales on WMAP and Planck foreground contaminated CMB maps at pixel resolution defined by HEALPix² pixel resolution parameter $N_{\text{side}} = 16$ and at a beam resolution of a Gaussian beam with FWHM = 9° . For completeness, in this article we briefly review the method. In the Gibbs ILC approach, we estimate the CMB posterior density, $P(\mathbf{S}, C_\ell | \mathbf{D})$ where \mathbf{S} is the true CMB signal, C_ℓ denotes the theoretical CMB angular power spectrum and \mathbf{D} is the given observed CMB data, by drawing samples of \mathbf{S} and C_ℓ from the distribution using Gibbs sampling technique (Larson et al. 2007; Eriksen et al. 2004, 2008; Groenboom

2009; Geman & Geman 1984). In Gibbs sampling at the beginning of any Gibbs iteration i , a CMB signal \mathbf{S}^{i+1} is sampled from the conditional density of \mathbf{S} , $P_1(\mathbf{S} | \mathbf{D}, C_\ell)$, given both observed data \mathbf{D} and a theoretical CMB angular power spectrum C_ℓ^i i.e.,

$$\mathbf{S}^{i+1} \leftarrow P_1(\mathbf{S} | \mathbf{D}, C_\ell^i). \quad (1)$$

Using the sampled CMB signal \mathbf{S}^{i+1} , a theoretical CMB angular power spectrum C_ℓ^{i+1} is sampled from the conditional density of C_ℓ , $P_2(C_\ell | \mathbf{D}, \mathbf{S})$, given both observed data \mathbf{D} and a CMB map, \mathbf{S}^{i+1} i.e.,

$$C_\ell^{i+1} \leftarrow P_2(C_\ell | \mathbf{D}, \mathbf{S}^{i+1}). \quad (2)$$

At the end of i^{th} iteration, one has a pair of \mathbf{S}^{i+1} and C_ℓ^{i+1} . These two steps are repeated large number of times where at each step C_ℓ^i in Eqn. 1 is replaced by C_ℓ^{i+1} of Eqn. 2 and similarly \mathbf{S}^{i+1} of Eqn. 2 by \mathbf{S}^{i+2} from new Eqn. 1. Removing some initial samples of \mathbf{S} and C_ℓ (the burn-in phase) all other samples in the sequence appear as if they are sampled from the joint CMB posterior density $P(\mathbf{S}, C_\ell | \mathbf{D})$ rather than their individual conditional probability distributions.

Since we intend to reconstruct the joint CMB posterior density in a foreground model independent manner we sample \mathbf{S} at each Gibbs iteration by minimizing the foregrounds present in the observed data using the global ILC method.

Let us assume that we have n number of mean subtracted foreground contaminated full-sky CMB maps \mathbf{X}_i , at a frequency ν_i , with $i = 1, 2, \dots, n$. Then a CMB estimate $\hat{\mathbf{S}}$ of the underlying true CMB signal \mathbf{S} is obtained by linearly combining these n input maps, i.e.,

$$\hat{\mathbf{S}} = \sum_{i=1}^n w_i \mathbf{X}_i, \quad (3)$$

where, w_i is the weight corresponding to the i^{th} frequency channel. To preserve the CMB signal in the cleaned map³ the weights follow a constrain that the sum of all the weights corresponding to n frequency channels should be unity i.e.,

$$\sum_{i=1}^n w_i = 1. \quad (4)$$

Using this condition on weights, we perform a constrained minimization of the CMB covariance weighted variance, $\sigma^2 = \hat{\mathbf{S}}^T \mathbf{C}^\dagger \hat{\mathbf{S}}$ where \mathbf{C} is the theoretical CMB covariance matrix (Sudevan & Saha 2018a,b) and \dagger represents the Moore-Penrose generalized inverse (Penrose 1955a,b), in order to estimate the weights. The choice of weights which minimizes σ^2 is obtained by following a Lagrange's multiplier approach,

$$\mathbf{W} = \frac{\hat{\mathbf{A}}^\dagger \mathbf{e}}{\mathbf{e}^T \hat{\mathbf{A}} \mathbf{e}}, \quad (5)$$

where, $\hat{A}_{ij} = \mathbf{X}_i^T \mathbf{C}^\dagger \mathbf{X}_j$, \mathbf{W} is an $(n \times 1)$ weight vector and \mathbf{e} is the $n \times 1$ shape vector of the CMB in thermodynamic temperature units. Typically, if the input CMB maps are calibrated correctly across all frequency channels, the shape vector is then an $(n \times 1)$ identity column vector, therefore $\sum_{i=1}^n w_i e_i = 1$.

² Hierarchical Equal Area Iso-Latitude Pixelation of Sphere which was developed by Górski et al. (2005).

³ Ignoring any spectral distortion CMB temperature anisotropy in thermodynamic temperature unit is independent on frequency.

The cleaned CMB map, $\hat{\mathbf{S}}$, estimated using the global ILC method is given by,

$$\hat{\mathbf{S}} = \mathbf{D}\mathbf{W} = \mathbf{D} \frac{\hat{\mathbf{A}}^\dagger \mathbf{e}}{\mathbf{e}^T \hat{\mathbf{A}}^\dagger \mathbf{e}}, \quad (6)$$

where, \mathbf{D} is a set of n observed CMB maps $(\mathbf{X}_1, \mathbf{X}_2, \dots, \mathbf{X}_n)$. Since over large angular scales (e.g., at pixel resolution $N_{\text{side}} = 16$ and beam smoothed by a Gaussian beam of FWHM $= 9^\circ$) the observed CMB maps have negligible detector noise levels, the global ILC weights adjust themselves in such a way that they cancel out the correlated foregrounds across frequency channels and while doing so they minimize the bad effects of CMB-foreground chance correlations as well, over large angular scales, thereby providing a cleaned CMB map $\hat{\mathbf{S}}$ very close to the true CMB signal, \mathbf{S} . Eqn. 5 shows the relation between global ILC weights, \mathbf{W} , and the CMB shape vector, \mathbf{e} .

3. BIAS IN PRESENCE OF RESIDUAL CALIBRATION ERROR

If in a CMB experiment, the observed CMB maps are not calibrated correctly, then in the presence of calibration uncertainties δe_i , corresponding to the CMB map observed in the frequency channel ν_i , the elements of CMB shape vector in thermodynamic temperature unit will be modified as $e'_i = 1 + \delta e_i$, or following a vector notation $\mathbf{e}' = \mathbf{e} + \delta \mathbf{e}$. If $\delta \mathbf{e}$ were completely known, the weights estimated using the new shape vector \mathbf{e}' , while minimizing the foregrounds in these observed maps, will still be subjected to the constraint that $\sum_{i=1}^n w_i e'_i = 1$ so that it will not introduce any multiplicative bias in the cleaned CMB amplitude. But in any CMB experiment, it is not possible to obtain the exact numerical values of calibration coefficients corresponding to the observed maps. Hence it is interesting to understand what will happen if we use Gibbs ILC method on those input maps with some level of calibration uncertainties in each map while (incorrectly) assuming the CMB shape vector to be the unit vector \mathbf{e} in Eqn. 5 (or in Eqn. 6).

In the presence of calibration error the cleaned map following Eqn. 3 is given by,

$$\hat{\mathbf{S}} = \sum_{i=1}^n \left(w_i e'_i \mathbf{S} + w_i e'_i \sum_{k=1}^{n_f} f_i^k \mathbf{F}_0^k \right), \quad (7)$$

where \mathbf{S} and \mathbf{F}_0^k respectively represents the true sky CMB signal and foreground template for the foreground component k at some reference frequency and n_f denotes the total number of foreground components⁴. The factor f_i^k represents the i^{th} element of the k^{th} foreground shape-vector \mathbf{f}^k . Defining, $\mathbf{g}_i^k = e'_i f_i^k$ we can write Eqn. 7 following the matrix notation as follows,

$$\hat{\mathbf{S}} = [\mathbf{W}^T \cdot \mathbf{e}'] \mathbf{S} + \left[\mathbf{W}^T \cdot \sum_{k=1}^{n_f} \mathbf{g}^k \right] \mathbf{F}_0^k. \quad (8)$$

Using this equation we note that in presence of calibration error the foreground shape vectors modifies to \mathbf{g}^k from initial \mathbf{f}^k without any alteration of total number of foreground components or the underlying foreground degrees of freedom. Using Eqn. 8 we can infer about presence of different kinds of bias in presence of calibration error as discussed below.

⁴ In Eqn. 7 we have assumed the detector noise is negligible, which is the case for WMAP and Planck observations for temperature anisotropy over large angular scales of the sky.

3.1. CMB Bias or Normalization Bias

Although, in presence of calibration error \mathbf{e}' enters in Eqn. 8 while estimating the weights using Eqn. 5, we assume that there are no calibration errors in the observed maps, i.e., we keep \mathbf{e} as a unit $n \times 1$ vector, hence, $[\mathbf{W}^T \cdot \mathbf{e}'] \neq 1$ in Eqn. 8.

This leads to CMB normalization bias in $\hat{\mathbf{S}}$. Depending upon whether $[\mathbf{W}^T \cdot \mathbf{e}'] > 1$ or < 1 the CMB map will be biased high or low than the sky CMB signal. We note that, even in presence of calibration error, if it so happens $[\mathbf{W}^T \cdot \delta \mathbf{e}] \sim 0$, then $[\mathbf{W}^T \cdot \mathbf{e}'] \sim [\mathbf{W}^T \cdot \mathbf{e}] = 1$. Hence, if random δe_i are such that $[\mathbf{W}^T \cdot \delta \mathbf{e}] \sim 0$ the net normalization bias in $\hat{\mathbf{S}}$ will be close to zero. A larger deviation of $[\mathbf{W}^T \cdot \delta \mathbf{e}]$ from 0 will lead to greater normalization bias in the cleaned map.

3.2. Foreground Bias

In the presence of calibration errors weights are expected to be dependent on $\delta \mathbf{e}$. This may cause weights to deviate from the optimal values which would have otherwise removed foregrounds satisfactorily in absence of the calibration error. It is interesting, therefore, to ask *how much foreground bias may be caused in the cleaned map due to calibration errors?* Following an analysis similar to Sudevan & Saha (2018b); Saha & Aluri (2016), we obtain,

$$\mathbf{W} = \frac{(\mathbf{I} - \mathbf{C}_f \mathbf{C}_f^\dagger) \mathbf{e}'}{\mathbf{e}'^T (\mathbf{I} - \mathbf{C}_f \mathbf{C}_f^\dagger) \mathbf{e}'} \left[1 + 2(\delta \mathbf{e})'^T \hat{\mathbf{A}}^\dagger \mathbf{e}' \right] - \frac{(\delta \mathbf{e})'^T \hat{\mathbf{A}}^\dagger}{\mathbf{e}'^T \hat{\mathbf{A}}^\dagger \mathbf{e}'}, \quad (9)$$

where \mathbf{I} represents the $n \times n$ identity matrix and \mathbf{C}_f follows,

$$\mathbf{C}_f = \sum_{\ell=2}^{\ell_{\text{max}}} \frac{2\ell+1}{C_\ell} \mathbf{C}_\ell^f, \quad (10)$$

as in Sudevan & Saha (2018b) and \mathbf{C}_ℓ^f represents the $n \times n$ empirical foreground covariance matrix in multipole space in observed data with calibration error. C_ℓ represents the theoretical CMB angular power spectrum. In zero order of the small calibration error $\delta \mathbf{e}$ Eqn. 9 reduces to

$$\mathbf{W} \sim \frac{(\mathbf{I} - \mathbf{C}_f \mathbf{C}_f^\dagger) \mathbf{e}'}{\mathbf{e}'^T (\mathbf{I} - \mathbf{C}_f \mathbf{C}_f^\dagger) \mathbf{e}'}. \quad (11)$$

We note that $\mathbf{C}_f \mathbf{C}_f^\dagger$ is a projector on the column space of \mathbf{C}_f , $\mathcal{C}(\mathbf{C}_f)$. Now following Sudevan & Saha (2018b), if $n > n_f$ then the null space of \mathbf{C}_f is a non-empty set and $(\mathbf{I} - \mathbf{C}_f \mathbf{C}_f^\dagger)$ is a projector on the null space. From Eqn. 11, we see that, the weight vector \mathbf{W} (which is actually estimated after incorrectly assuming CMB shape vector to be a unit vector, \mathbf{e} in Eqn. 5) satisfies

$$\mathbf{W}^T \mathbf{g}_k \sim 0 \quad \forall \quad k, \quad (12)$$

since \mathbf{g}^k lies completely inside the column space of \mathbf{C}_f . Since any deviation of $\mathbf{W}^T \mathbf{g}_k$ from zero (for any k) causes foreground residual in the cleaned map, Eqn. 12 implies that, *if the residual calibration error of the input maps are small, there will be only very small residual foreground bias in the foreground cleaned CMB map even if the weights are estimated assuming no calibration error in the input maps.*

Frequency map	K1	30 GHz	Ka1	Q	44GHz	V	70 GHz	W	100 GHz	143 GHz	217 GHz	353 GHz
Calibration error, σ_c , (%)	0.2	0.17	0.2	0.2	0.12	0.2	0.2	0.2	0.08	0.021	0.028	0.024

Table 1 - Table contains the level of residual calibration error (in %) in the CMB maps provided by the WMAP and Planck satellite missions.

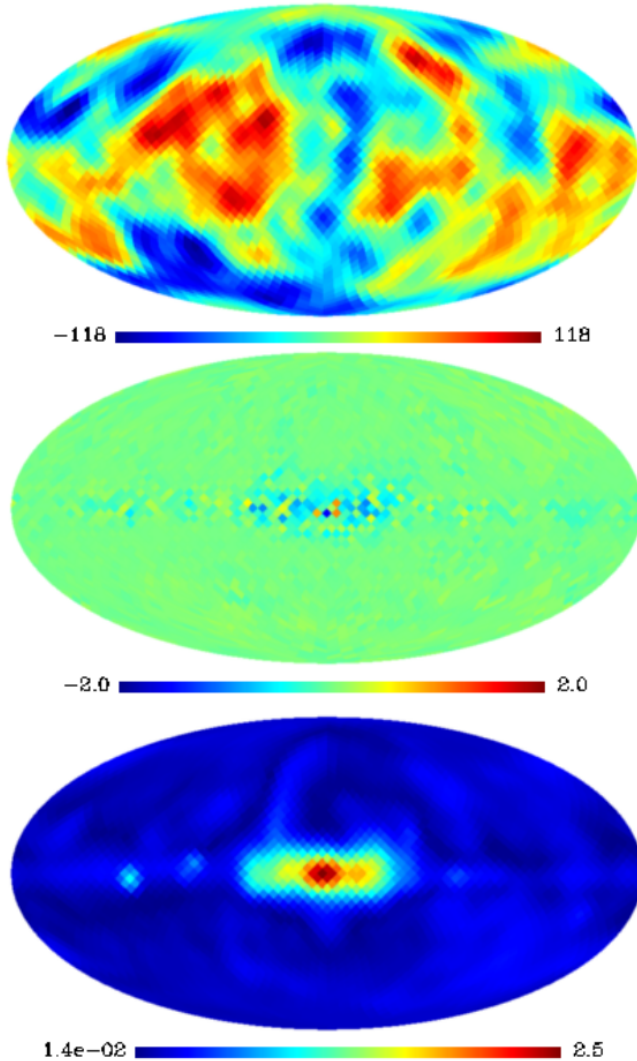


FIG. 1.— In the top panel, we show the mean of the best-fit cleaned CMB maps obtained from our 1000 Monte Carlo simulations using different set of input simulated foreground contaminated maps with random calibration errors consistent with Planck and WMAP CMB observations. We show the difference between the mean best-fit cleaned CMB map and the best-fit cleaned CMB map obtained from the simulation without any calibration errors in the middle panel. We see that both the maps agrees well with each other and there is only a minor difference of $2.5\mu K$ in the galactic region. In the bottom panel, the standard deviation of all the 1000 best-fit cleaned CMB maps are shown.

4. METHODOLOGY

The Planck consortium after using advanced photometric calibration techniques like spin-synchronous modulation of the CMB orbital dipole for Low-Frequency instrument (LFI) and by using models of planetary atmospheric emissions and time-variable CMB orbital dipole for High-Frequency Instrument (HFI) maps, has dramatically brought down the calibra-

tion uncertainties in the Planck full-sky surveys. However, since it is impossible to determine the exact value of the calibration coefficient corresponding to each individual map, performing detailed Monte Carlo simulations, where we simulate foreground and detector noise contaminated maps which mimic the real-life observed CMB maps, is the only way to understand the impact of using incorrect calibration coefficients during a CMB reconstruction method.

In the current analysis we perform 1000 different sets of Monte Carlo simulations of entire Gibbs ILC procedure for a comprehensive study of the impact of using input frequency maps with varying level of (residual) calibration errors corresponding to different simulation sets, on the Gibbs ILC results. The calibration errors used in these simulations are consistent with the WMAP (Bennett et al. 2013; Jarosik et al. 2011) and Planck 2018 results (Akrami et al. 2018; Aghanim et al. 2018a). We mention the calibration error levels in table 3.1 assuming they represent 1σ error levels.

In these Monte Carlo simulations, in each set, we simulated foregrounds and detector noise contaminated CMB maps at all WMAP and Planck frequency channels at a pixel resolution $N_{side} = 16$ and beam smoothed by a Gaussian beam of FWHM 9° . The free-free, synchrotron and thermal dust emissions at different frequency channels are obtained at $N_{side} = 256$ and at beam resolution 1° following the procedure as described in Sudevan et al. (2017). These maps are then downgraded to $N_{side} = 16$ and performed an additional smoothing by a Gaussian beam of FWHM $= \sqrt{540^2 - 60^2}$ to bring all the foreground maps to 9° beam smoothing. We generated a CMB temperature map using the theoretical CMB power spectrum consistent with cosmological parameters obtained by Planck collaboration Ade et al. (2016c) at $N_{side} = 16$ and beam smoothing of 9° . We follow the same procedure given in Sudevan et al. (2017) to generate detector noise maps corresponding to each input map at $N_{side} = 16$ and 9° smoothing, the detector noise levels being in accordance with the estimate provided by WMAP and Planck science team. The final simulated foreground contaminated maps at different Planck and WMAP frequencies are obtained by linearly combining the CMB, various foregrounds and the detector noise maps.

Once we simulated these input maps, they are then scaled by calibration factors obtained by randomly drawing a unit mean Gaussian random variable x_i , where $i = 1, \dots, n$ (total number of maps), with standard deviation equal to the desired amount of calibration error mentioned in Table 3.1. This generates a given set of input maps with the randomly chosen calibration errors. For the purpose of Monte Carlo simulations we simulate a total of 1000 different sets of input maps with random calibration errors.

After simulating the foreground contaminated maps with different levels of calibration error for different sets, we use Gibbs ILC algorithm to minimize the foregrounds. While implementing Gibbs ILC code, we assumed that all the input simulated maps are calibrated equally i.e., the shape vector is

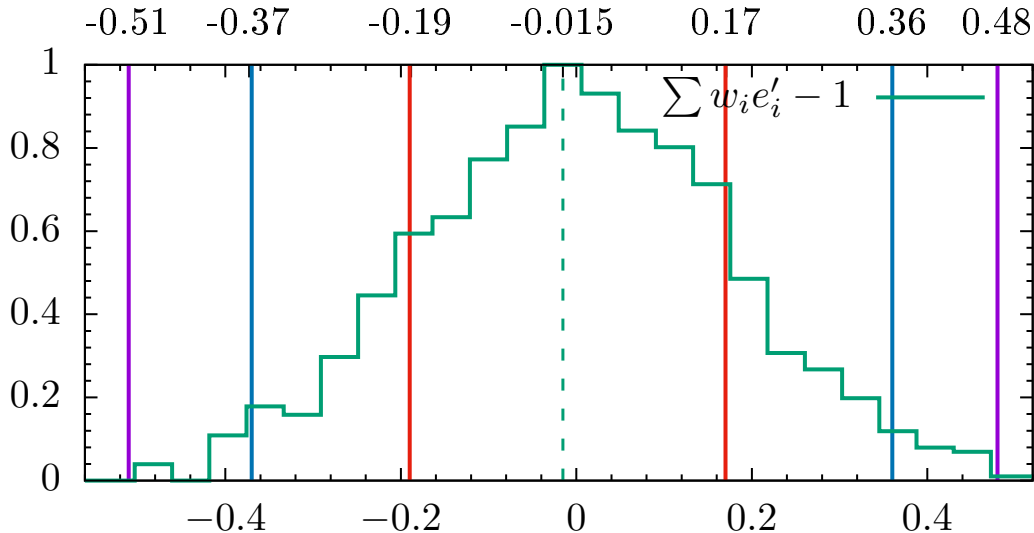


FIG. 2.— Figure showing the distribution of CMB normalization bias, $\sum_{i=1}^n w_i e_i' - 1$, in percentage level corresponding to the 1000 sets of CMB reconstruction using the Gibbs ILC method. We see that the mode of the distribution is centered around -0.015% which translates into about $\pm 0.00018\mu\text{K}$ difference in the temperature at each pixel at 1σ level.

a unit vector, \mathbf{e} . In the current implementation of Gibbs ILC procedure, each simulation consists of 10 chains each with randomly chosen initial points and 5000 Gibbs steps. We reject 50 samples (each from cleaned CMB maps and sampled CMB theoretical angular power spectra) corresponding to initial burn-in phase. This results in a total of 49500 samples from each simulation.

5. RESULTS

In this section, we discuss the results obtained after performing detailed Monte Carlo simulations of CMB reconstruction using 1000 different sets of input maps with random calibration errors consistent with WMAP and Planck observations. While implementing the Gibbs ILC method, during the foreground minimization using the global ILC method we do not take into account of the presence of calibration errors in the map. We follow the same procedure as outlined in Sudevan & Saha (2018b) for calculating the CMB posterior, best-fit CMB map and best-fit theoretical CMB angular power spectrum from the cleaned CMB map and theoretical angular power spectrum samples generated.

5.1. Cleaned Maps

Using 49500 sampled maps from a given set of simulations we estimate the best-fit CMB map corresponding to the maximum likely pixel values for each pixel. Using best-fit CMB maps from all 1000 simulation sets we estimate a simple mean map. In Fig. 1, we show the mean best-fit cleaned CMB map in the top panel. This map agrees very well with the best-fit CMB map when the simulation involved no calibration error in input maps. This is shown in the middle panel of Fig. 1. Minor difference of $\sim \pm 2\mu\text{K}$ is seen only in the central galactic plane. The bottom panel of this figure shows the standard deviation map computed from 1000 best-fit CMB maps. From the standard deviation map we see that maximum error occurs in the central galactic region of magnitude $\sim 2.5\mu\text{K}$. Using these results we therefore conclude that even in the presence of realistic levels of residual calibration error in the input frequency maps the Gibbs ILC method performs very well in CMB reconstruction. The resulting residual foreground con-

tamination due to any unaccounted for calibration error is limited to $\sim \pm 6\mu\text{K}$ with a 3σ confidence level only along the very central region of the galactic plane.

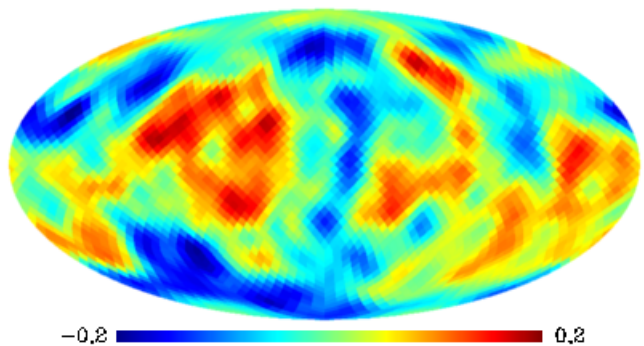


FIG. 3.— Figure showing the normalization bias in the CMB map corresponding to the 1σ level of $\sum w_i e_i' - 1$. We see that at 1σ of normalization bias the maximum change in pixel temperature is of the order of $\pm 0.2\mu\text{K}$.

Apart from the small level of residual foreground bias due to residual calibration error in input frequency maps as discussed above the cleaned CMB maps contain a CMB normalization bias for the same reason (e.g., see Section 3.2 and 3.1). The normalization bias arises since in case of input frequency maps with calibration errors weights should have satisfied $\mathbf{W}^T \mathbf{e}' = 1$ to preserve the amplitude of the CMB component in the cleaned map, whereas, they satisfy $\mathbf{W}^T \mathbf{e} = 1$, where $\mathbf{e}' = \mathbf{e} + \delta\mathbf{e}$ and $\delta\mathbf{e}$ represents the unknown residual calibration error. A measure of the normalization bias in any given experiment with a given set of unknown residual calibration error is then $\mathbf{W}^T \mathbf{e}' - 1$. We show the distribution of CMB normalization bias in percentage level using 1000 sets of CMB reconstruction using the Gibbs ILC method in Fig. 2. As seen from this figure the normalization bias is only 0.17% at 1σ level in a CMB reconstruction method using Gibbs ILC method. In Fig. 3 we show the normalization bias map for the chosen input CMB map of this work corresponding to 1σ value of $\sum w_i e_i' - 1$. For the calibration error levels of WMAP and Planck the normalization bias is less than $0.2\mu\text{K}$ in mag-

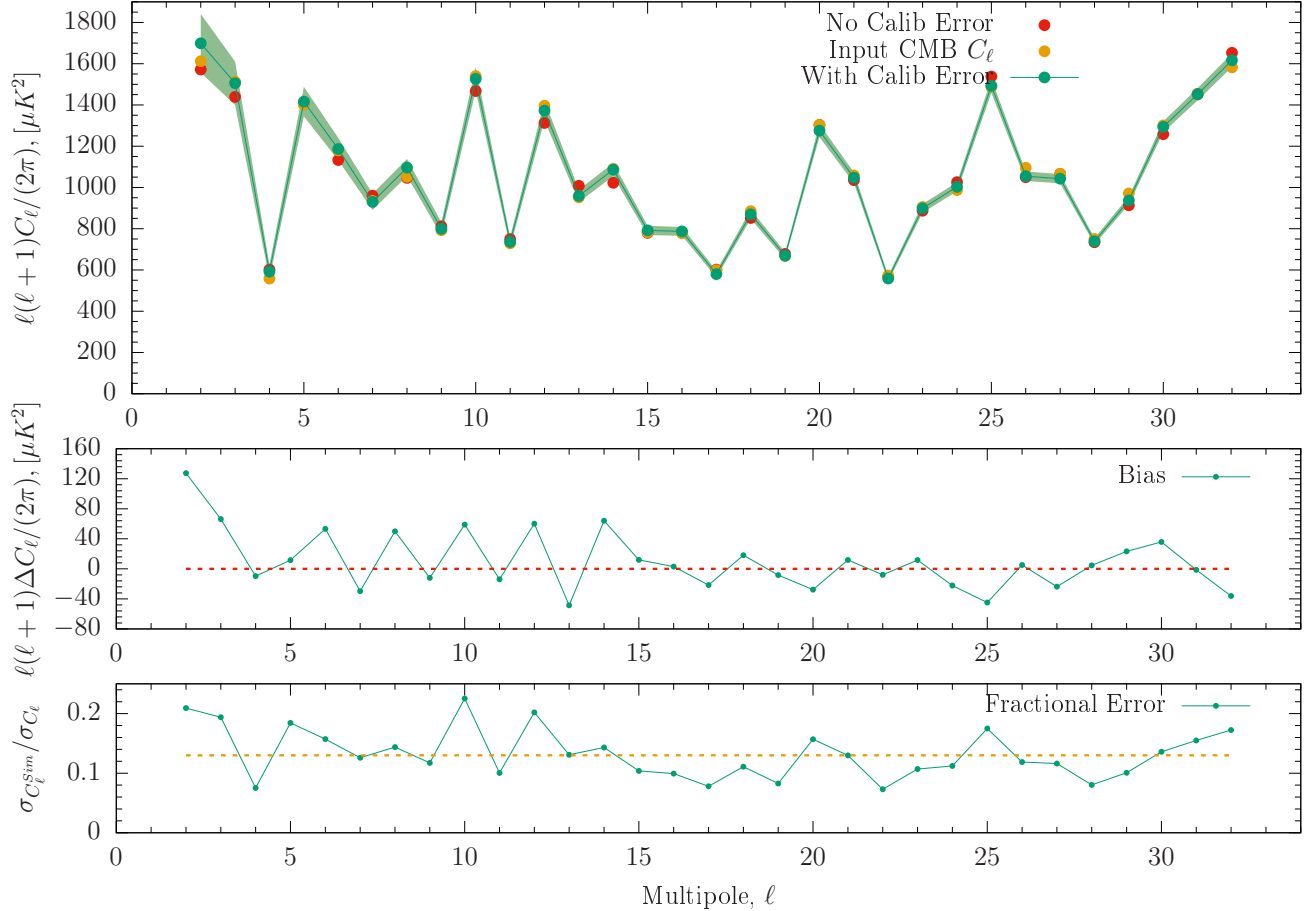


FIG. 4.— In the top panel, we show the mean best-fit estimated from all the 1000 Monte Carlo simulations using green line. The best-fit theoretical angular power spectrum obtained from simulation with no calibration error is shown using red points and the input CMB angular power spectrum used in all the simulations is shown using yellow points. The 1σ standard deviation region corresponding to the best-fits from the Monte Carlo simulations is shown as a light green shaded region around the mean best-fit angular power spectrum. We see from this plot that the mean best-fit agrees well with both the input CMB and best-fit (from no calibration errors simulation) angular power spectrum. Both the input CMB angular power spectrum and best-fit angular power spectrum lie inside the 1σ region of the mean best-fit. In the middle panel we show the difference of mean best-fit angular power spectrum where calibration error was included in the simulations and best fit spectrum without any calibration error. The bottom panel compares the standard deviations of the best-fit spectra with calibration error with the cosmic variance. The calibration induced errors appear to be approximately uniformly distributed over multipoles with respect to the cosmic variance induced errors. Yellow line represents the mean fractional error of 13% between the entire multipole range.

nitide.

5.2. Best-fit CMB angular power spectrum

Since exact values of calibration coefficients are unknown in any CMB experiment estimated values of best-fit CMB angular power spectrum would be different from the actual ones that would have been estimated in the hypothetical case when the calibration coefficients would be exactly known. Such differences may result in a bias in the estimated best-fit CMB angular power spectrum apart from causing larger errors in the later due to random nature of the calibration uncertainties. Using 1000 Monte Carlo simulations of CMB posterior estimations using the Gibbs ILC method in this section we assess this bias and error in the best-fit CMB angular power spectrum in presence of calibration uncertainties.

In order to understand any possible bias in the best-fit CMB power spectrum in Gibbs ILC method due to residual calibration error we show in top panel of Fig. 4 the mean best-fit CMB angular power spectrum obtained from 1000 simulations (in green) with calibration errors along with the best-fit angular power spectrum when the input frequency maps contained no calibration error (in red). The green filled region

around the mean best-fit angular power spectrum represents the 1σ error levels at different multipoles obtained from 1000 best-fit angular power spectra. The mean best-fit with calibration error matches very well with the zero calibration error case. In the middle panel of this figure we show any bias in the best-fit angular power spectrum with respect to the zero calibration error case by plotting the difference of mean best-fit CMB angular power spectrum (with calibration error) and best-fit spectrum without any calibration error. Visually the differences take more positive values between $\ell = 2$ and $\ell = 15$, whereas, differences take somewhat more negative values between $\ell = 16$ to $\ell = 32$. The average bias in the first multipole range is as small as $\sim 28\mu K^2$. Average bias between $\ell = 16$ to $\ell = 32$ is just $-4.7\mu K^2$. In the bottom panel of Fig. 4 we show the calibration uncertainty induced error in the best-fit CMB angular power spectrum by plotting the ratio of standard deviations ($\sigma_{C_\ell^{sim}}$) of the best-fit spectra in presence of calibration error and cosmic variance induced error (σ_{C_ℓ}). The standard deviation from simulations varies between 8% (at $\ell = 4$) and a maximum of 22% at $\ell = 10$ of cosmic variance induced error. Calibration induced mean fractional error between $\ell = 2$ and $\ell = 32$ is just 13%. The calibration error

induced error is expected to add in quadrature with the cosmic variance induced error. Considering this mean level of fractional error net error becomes $\sqrt{1+0.13} = 1.06$ times of the cosmic variance induced error. This causes a 6% error increase from the cosmic variance prediction between multipole range $2 \leq \ell \leq 32$.

Summarizing the simulation results of this section, we conclude that even in the presence of calibration uncertainties in the input foreground and detector noise contaminated CMB maps, our Gibbs ILC method produces a best-fit cleaned CMB map which has very minor level of residual foreground contamination bias and an almost negligible CMB normalization bias. For the best-fit power spectrum calibration induced bias and error both remain small.

6. CONCLUSIONS & DISCUSSIONS

The level of calibration uncertainties present in the observed CMB maps have been drastically reduced by following advanced photometric calibration techniques like spin-synchronous modulation of the CMB orbital dipole Adam et al. (2016a); Ade et al. (2016b); Akrami et al. (2018), by using models of planetary atmospheric emissions Adam et al. (2016b); Aghanim et al. (2018a) etc. But the presence of the residual calibration error (however small it be) in the observed CMB maps may pose a difficult challenge while estimating a pure CMB signal. In the current article, we study the impact of random calibration errors on the CMB map and its angular power spectrum that are obtained using Gibbs ILC method. Since it is impossible to obtain the exact value of calibration uncertainties corresponding to each individual observed CMB maps, we therefore, perform detailed Monte Carlo simulations of Gibbs ILC method with realistic residual calibration errors compatible to WMAP and Planck observations, after simulating realistic foreground and detector noise contaminated CMB maps over large angular scales of the sky.

Using analytical results we show in Section 3 that residual errors in calibration coefficients lead to two distinct type of bias in Gibbs ILC method which is implemented over large angular scales of the sky. The first kind of bias is called the CMB normalization bias which arises since the empirical weights satisfy $\mathbf{W}^T \mathbf{e} = 1$ instead of $\mathbf{W}^T \mathbf{e}' = 1$, where \mathbf{e}' represents the true CMB shape vector in presence of calibration error. The second type of bias is due to residual foreground contamination in the cleaned maps. By estimating best-fit cleaned CMB maps corresponding to the maximum of the posterior

density by detailed Monte Carlo simulations, in Sec. 5, the normalization bias is merely 0.17% at a confidence level of 1σ . The residual foreground bias is small as well. Our Monte Carlo simulations show that the residual calibration error tend to maximally bias only the galactic central region, with a magnitude of $\sim 2\mu K$ at 1σ confidence level. Between $2 \leq \ell \leq 15$ (mean) bias in the best-fit CMB angular power spectrum when calibration errors are present in the input maps in Gibbs ILC method is $\sim 28\mu K^2$ with respect to the ideal case of zero calibration error. This bias decreases with increase in multipoles, and is just $-4.7\mu K^2$ between $16 \leq \ell \leq 32$. The calibration error widens the error intervals on the best-fit CMB angular spectrum. The average increase of net error level between $2 \leq \ell \leq 32$ is $\sim 6\%$ over the cosmic variance induced error.

Based upon our Monte Carlo simulations we conclude that for an analysis over large angular scales of the sky, even if we use the maps with realistic (residual) calibration errors without accounting for the same in the Gibbs ILC algorithm (by modifying the CMB shape vector) leads to very minor level of bias in the best-fit cleaned CMB map. The bias and error in the best-fit CMB angular power spectrum are both small, however, they may not completely negligible. It would be important to incorporate such bias and error in the angular power spectrum in cosmological parameter estimation and investigate their role in cosmological parameter estimation.

Finally, we mention an interesting advantage of the Gibbs ILC method on the issue of impact of residual calibration errors on the CMB reconstruction. Since our method does not require to model the frequency spectrum nor any templates for foreground components to reconstruct the CMB products to a good accuracy our foreground removal is independent on the calibration error, as long as the later is small (e.g., Section 3.2).

This work is based on observations obtained with Planck (<http://www.esa.int/Planck>) and WMAP (<https://map.gsfc.nasa.gov/>). Planck was an ESA science mission with instruments and contributions directly funded by ESA Member States, NASA, and Canada. We acknowledge use of Planck Legacy Archive (PLA) and the Legacy Archive for Microwave Background Data Analysis (LAMBDA). LAMBDA is a part of the High Energy Astrophysics Science Archive Center (HEASARC). HEASARC/LAMBDA is supported by the Astrophysics Science Division at the NASA Goddard Space Flight Center. We use publicly available HEALPix Górski et al. (2005) package (<http://healpix.sourceforge.net>) for the analysis of this work.

REFERENCES

- Adam, R., et al. 2016a, *Astron. Astrophys.*, 594, A1
 —. 2016b, *Astron. Astrophys.*, 594, A8
 Ade, P. A. R., et al. 2016a, *Astron. Astrophys.*, 594, A18
 —. 2016b, *Astron. Astrophys.*, 594, A5
 —. 2016c, *Astron. Astrophys.*, 594, A13
 Aghanim, N., et al. 2018a, arXiv:1807.06207
 —. 2018b, arXiv:1807.06209
 Akrami, Y., et al. 2018, arXiv:1807.06206
 André, P., Baccigalupi, C., Banday, A., et al. 2014, *Jour. Cosmol. Astro. Phys.*, 2014, 006
 Bennett, C. L., et al. 2003, "*Astrophys. J. Suppl.*", 148, 97
 Bennett, C. L., Larson, D., Weiland, J. L., et al. 2013, *ApJS*, 208, 20
 Di Valentino, E., et al. 2018, *JCAP*, 1804, 017
 Dick, J., Remazeilles, M., & Delabouille, J. 2010, *MNRAS*, 401, 1602
 Eriksen, H. K., Jewell, J. B., Dickinson, C., et al. 2008, *Astrophys. J.*, 676, 10
 Eriksen, H. K., et al. 2004, *Astrophys. J.*, 612, 633
 Eriksen, H. K., et al. 2004, *Astrophys. J. Suppl.*, 155, 227
 Fixsen, D. J., et al. 1996, "*Astrophys. J.*", 473, 576
 Geman, S., & Geman, D. 1984, *IEEE Trans. Pattern Anal. Mach. Intell.*, 6, 721
 Goldstein, J. H., et al. 2003, *Astrophys. J.*, 599, 773
 Górski, K. M., Hivon, E., Banday, A. J., et al. 2005, *ApJ*, 622, 759
 Groeneboom, N. E. 2009, ArXiv e-prints, arXiv:0905.3823
 Hanany, S., et al. 2019, arXiv:1902.10541
 Hinshaw, G., et al. 2003, *Astrophys. J. Suppl.*, 148, 63
 —. 2007, *Astrophys. J. Suppl.*, 170, 288
 Hinshaw, G., et al. 2013, *Astrophys. J. Suppl.*, 208, 19
 Jarosik, N., Bennett, C. L., Dunkley, J., et al. 2011, *ApJS*, 192, 14
 Kogut, A., Chluba, J., Fixsen, D. J., Meyer, S., & Spergel, D. 2016, *Society of Photo-Optical Instrumentation Engineers (SPIE) Conference Series*, Vol. 9904, *The Primordial Inflation Explorer (PIXIE)*, 99040W
 Kogut, A., et al. 2011, *Journal of Cosmology and Astro-Particle Physics*, 2011, 025

- Larson, D. L., et al. 2007, *Astrophys. J.*, 656, 653
- Mather, J. C., et al. 1994, "*Astrophys. J.*", 420, 439
- Penrose, R. 1955a, in , 406–413
- Penrose, R. 1955b, *Mathematical Proceedings of the Cambridge Philosophical Society*, 51, 406
- Saha, R. 2011, *Astrophys. J. Lett.*, 739, L56
- Saha, R., & Aluri, P. K. 2016, *Astrophys. J.*, 829, 113
- Saha, R., Jain, P., & Souradeep, T. 2006, *Astrophys. J.*, 645, L89
- Sudevan, V., Aluri, P. K., Yadav, S. K., Saha, R., & Souradeep, T. 2017, *Astrophys. J.*, 842, 62
- Sudevan, V., & Saha, R. 2018a, *Astrophys. J.*, 867, 74
- . 2018b, arXiv:1810.08872
- Sutin, B. M., et al. 2018, *Proc. SPIE Int. Soc. Opt. Eng.*, 10698, 106984F
- Tegmark, M., & Efstathiou, G. 1996, *Mon. Not. Roy. Astron. Soc.*, 281, 1297
- Tegmark, M., et al. 2003, *Phys. Rev.*, D68, 123523